Batteries & Supercaps

Research Article
doi.org/10.1002/batt.202300089

Chemistry
Europe
European Chemical
Societies Publishing

www.batteries-supercaps.org

High Energy Density Li/Ni/Co-Free O3/P2 Sodium Layered Oxide Intergrowth for Sodium-Ion Batteries

Philip A. Maughan,[a, b] Aaron B. Naden,[a] John T. S. Irvine,[a, b] and A. Robert Armstrong*[a, b]

Sodium-ion batteries have attracted widespread interest due to the potential for providing safe and cheap energy storage. However, large scale use of sodium-ion batteries is limited by insufficient performance from positive electrode materials, while also avoiding the use of expensive and toxic elements. Here, we present a bi-phasic sodium layered oxide material, O3/P2-$Na_{0.75}Mn_{0.35}Fe_{0.35}Ti_{0.1}Al_{0.1}Cu_{0.1}O_2$, free of Li, Ni, and Co, which delivered high energy densities up to 420 Wh kg^{-1}, discharge potential of 3.03 V, and high capacity retention of 80 % over 70 cycles in half cells (292 Wh kg^{-1} in full cells). Crucially, the high Na content is sufficient to provide high energy densities in full cell format. The intergrown nature of the material was confirmed by TEM and SAED analysis, while ex-situ XRD studies revealed the two phases undergo complementary c-parameter evolution, reducing overall volume change. These results demonstrate the potential for future commercialisation of bi-phasic materials utilizing only Earth abundant elements.

Introduction

Sodium-ion batteries (SIBs) have emerged as a leading complement to lithium-ion batteries due to the low cost, widespread precursor availability and safety advantages compared to lithium-ion technology, which has led to promise in applications such as grid storage and lower performance electric vehicles.[1–3] However, widespread commercialization of SIBs is currently prevented by a lack of suitable positive electrode materials based on cheap Earth abundant elements which can deliver high energy densities and long cycling lifetimes, with current leading compositions utilising elements such as Ni ($Na_xMn_aNi_bTi_cMg_dO_2$, Faradion Ltd.) and vanadium ($Na_3V_2(PO_4)_2F_3$, Tiamat).

Sodium layered metal oxides (SLMO), Na_xTMO_2, which crystallize into two common polymorphs known as P2 and O3,[4] demonstrate high promise as positive electrode materials due to the versatile chemistry, high capacities and high tap density. These two polymorphs display complementary properties, where in the P2 structure Na occupies prismatic sites, which facilitates fast Na diffusion, but energy densities are limited by low Na contents (typically $x = 2/3$).[5] In contrast, the O3 phase accommodates high Na contents (up to $x = 1$), enabling high energy densities, but suffers from more complex phase transitions, poorer capacity retention and reduced rate performance.[6] In addition, the best performing SLMOs are typically based on nickel chemistry, which is undesirable due to the higher cost and toxicity of Ni.[5,7–10]

Therefore, to keep the cost of next-generation SIBs low, it is crucial to focus on the utilization of cheap, Earth abundant elements such as Mn and Fe in O3-$NaMn_{0.5}Fe_{0.5}O_2$ and P2-$Na_{0.67}Mn_{0.5}Fe_{0.5}O_2$.[11,12] However, both phases suffer from low charge capacities (110–125 mAh g^{-1}) and rapid capacity fade. To address this, substantial research focus has been applied to various dopants to improve the performance. Amongst these, Cu has shown particular promise due to the active Cu^{2+}/Cu^{3+} redox couple, which can provide extra high voltage capacity, enhance the rate capability of materials and reduce undesirable Fe migration.[13–15]

Consequently, multiple studies have been carried out on various Mn–Fe–Cu oxides to investigate their potential for Na-ion batteries.[15,16] Xu et al. studied P2-type $Na_{0.7}[Cu_{0.15}Fe_{0.3}Mn_{0.55}]O_2$ which showed a capacity of 98 mAh g^{-1} with ca. 80 % capacity retention over 80 cycles.[7] Li et al. synthesized P2-$Na_{7/9}Cu_{2/9}Fe_{1/9}Mn_{2/3}O_2$ which returned a discharge capacity of 89 mAh g^{-1} with an average voltage of 3.6 V.[17] Similar performance was observed for O3-$Na_{0.90}Cu_{0.22}Fe_{0.30}Mn_{0.48}O_2$, which showed initial capacities of 100 mAh g^{-1} (3.2 V).[18] Tripathi et al. used Ti doping to create O3-$Na_{0.9}Cu_{0.22}Fe_{0.30}Mn_{0.43}Ti_{0.05}O_2$ which raised the average voltage (to 3.38 V) and enhanced the capacity (from 85 mAh g^{-1} to 90 mAh g^{-1}).[19] Nevertheless, these single phase Mn–Fe–Cu oxides have all suffered from low initial capacities ($<$ 100 mAh g^{-1}), which despite high discharge potentials ($>$ 3.0 V), severely limit the available energy densities.

One strategy to overcome these performance issues is to combine both phases into one material. However, most previously reported O3/P2 bi-phasic materials have reported either low Na contents, use of expensive or unsustainable

[a] Dr. P. A. Maughan, Dr. A. B. Naden, Prof. J. T. S. Irvine, Dr. A. R. Armstrong
School of Chemistry
University of St Andrews
St Andrews, Fife, KY16 9ST (United Kingdom)
E-mail: ara@st-andrews.ac.uk
[b] Dr. P. A. Maughan, Prof. J. T. S. Irvine, Dr. A. R. Armstrong
The Faraday Institution
Quad One, Harwell Science and Innovation Campus
Didcot, OX11 0RA (United Kingdom)

elements such as Li and Ni, or both. For example, Lee et al. studied the series $Na_{1-x}Li_xNi_{0.5}Mn_{0.5}O_2$ (where $0 < x < 0.3$), which proved the existence of intergrown O3/P2 materials, but suffered from low capacities (ca. 120 mAh g^{-1}), and significant fade was seen even after only 20 cycles.[20] Other mixed-phase materials including O3/P2-$Na_{0.66}Li_{0.18}Mn_{0.71}Ni_{0.21}Co_{0.08}O_{2+\delta}$,[21] $Na_{0.67}Mn_{0.55}Ni_{0.25}Ti_{0.2-x}Li_xO_2$,[22] and $Na_{0.78}Ni_2Fe_{0.38}Mn_{0.42}O_2$, also have limited capacities below 100 mAh g^{-1}.[23–25] Yang et al. reported the O3-rich (60% O3) O3/P2 mixed phase material $Na_{0.8}Li_{0.2}Fe_{0.2}Mn_{0.6}O_2$ with high capacities up to 174 mAh g^{-1}, and good cycling stability of 82% retention over 100 cycles.[26] However, the polarisation was large (600 mV), and the use of Li is not practical for commercial SIBs, due to the highly volatile cost and limited supply of Li, which are main motivations for the adoption of Na-ion batteries. Consequently, there is still no report to-date of a material with high energy densities and stable cycling behaviour based on low cost, abundant elements.

In this work, we design a high energy density O3/P2 bi-phasic material based exclusively on low cost, Earth abundant and non-toxic elements, O3/P2-$Na_{0.75}Mn_{0.35}Fe_{0.35}Ti_{0.1}Al_{0.1}Cu_{0.1}O_2$, with high Na content compared to traditional P2 materials ($x = 0.75$), where the P2 part of the material stabilises the long-term cycling. This resulted in a high discharge capacity of 140 mAh g^{-1} (charge capacity of 166 mAh g^{-1}) and a suitable high discharge potential (3.03 V) which enabled a high discharge energy density of 419 Wh kg^{-1}$_{activePositiveMaterial}$, while maintaining stable cycling performance with a capacity retention of 80% over 70 cycles. The structure of the material was carefully characterised by a combination of diffraction and microscopy methods, while the cycling behaviour was studied in detail by ex-situ X-ray diffraction, the understanding of which allows for further improvements in battery performance by enabling the rational design of future positive electrode materials.

Results and Discussion

The crystal structure of the synthesised O3/P2 bi-phasic material, $Na_{0.75}Mn_{0.35}Fe_{0.35}Ti_{0.1}Al_{0.1}Cu_{0.1}O_2$, was investigated by laboratory powder X-ray diffraction (XRD), which demonstrated that the characteristic peaks for both the P2 (space group P6$_3$/mmc) and O3 (space group R$\bar{3}$m) type crystal structures are present in the material (Figure 1). This is further confirmed by Rietveld refinement analysis, which confirmed the successful synthesis of an O3/P2 bi-phasic material with the O3:P2 phase ratio quantified as 88:9 (a 3% impurity of b-Na(Fe,Al)O$_2$ was also detected). The refinement also revealed that the P2 phase had a slightly smaller a parameter compared to the O3 phase ($a = 2.9416(5)$ Å for the O3 phase and 2.9239(5) Å for the P2 phase), while the d-spacing between Na layers, calculated from the c parameter, was larger for the P2 phase, with d-spacings of 5.54 Å for O3 and 5.59 Å for the P2 phase, which is typical for previously reported P2 and O3 phases ($c = 16.616(5)$ Å for O3, which contains three layers per unit cell, and 11.174(3) Å for P2, which contains two layers per unit cell). Further details on the Rietveld refinement can be found in Supporting Information.

Scanning electron microscopy (SEM) was used to study the morphology and particle size of the bi-phasic composite
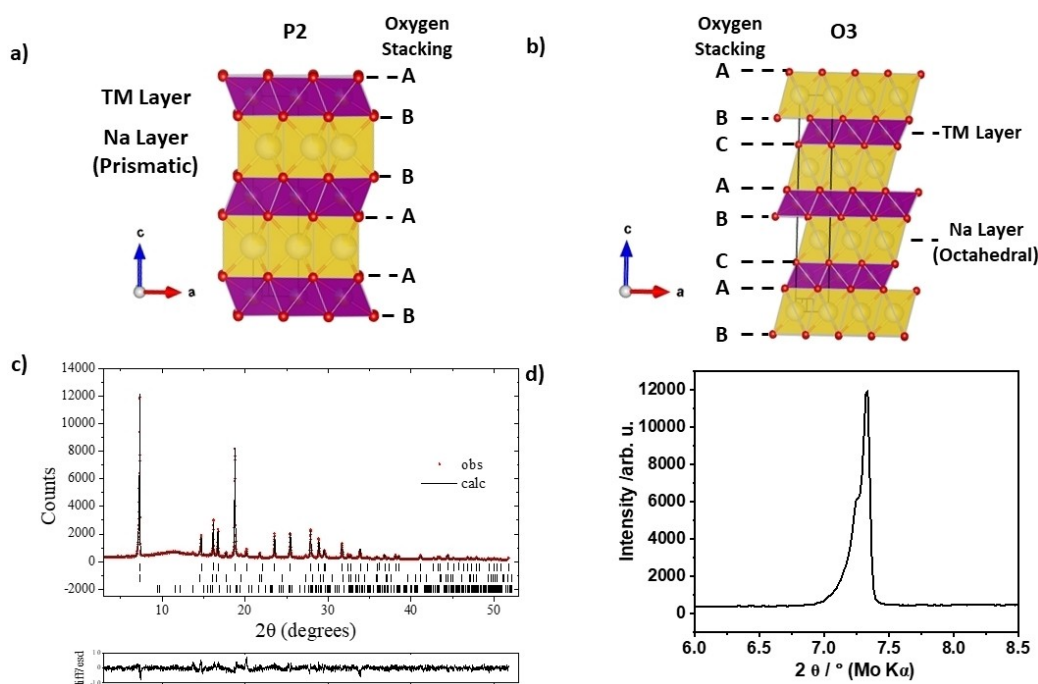
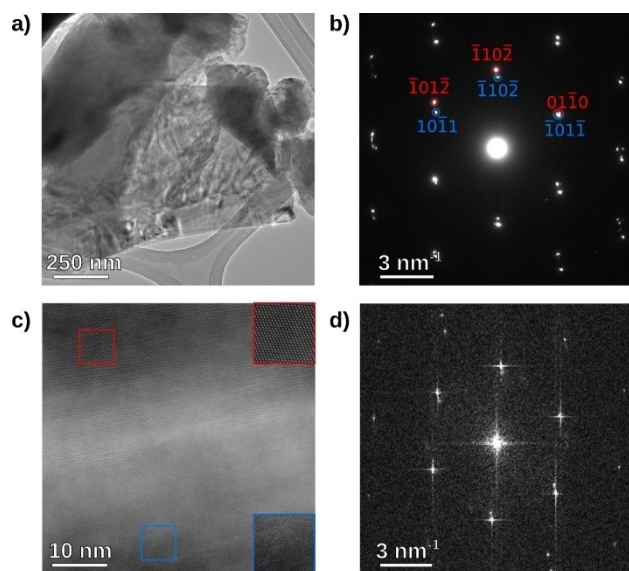**Figure 1.** a, b) Schematic diagram of typical a) P2 and b) O3 crystal structures. c) Rietveld refinement for the O3/P2 material. Observed data are shown by red dots, with the fitted profile in black. Tick marks indicate allowed reflections (O3 phase-top, P2 phase-middle, Na$_x$(Fe,Al)O$_2$ impurity-bottom). Lower panel shows difference/esd. d) Expanded view of the low angle region of the XRD pattern.

Batteries & Supercaps

Research Article
doi.org/10.1002/batt.202300089

Chemistry
Europe
European Chemical
Societies Publishing

Table 1. Synthesised materials with their sample names, chemical composition and phase composition.

Sample Name	Target chemical composition	Actual chemical composition (ICP)	Phase composition (Refinement, O3:P2 ratio)
O3/P2	$Na_{0.75}Mn_{0.35}Fe_{0.35}Ti_{0.1}Al_{0.1}Cu_{0.1}O_2$	$Na_{0.82}Mn_{0.35}Fe_{0.36}Ti_{0.08}Al_{0.10}Cu_{0.11}O_2$	88:9

(Figure S1). The particles display a smooth morphology, with sizes ranging from ca. 0.5 to 2 μm, while small secondary particles with dimensions of ca 100–200 nm can also be observed. SEM-EDS analysis suggests that these secondary particles are Al_2O_3 (Figure S2). Very small nanocrystals on the surface of some micron sized particles can also be observed, which are consistent with Na_2CO_3, trace quantities of which typically form in the synthesis of sodium layered oxides. Overall quantification of the SEM-EDS data is consistent with the target composition of $Na_{0.75}Mn_{0.35}Fe_{0.35}Ti_{0.1}Al_{0.1}Cu_{0.1}O_2$, albeit with a slight Al deficiency, which is confirmed by ICP-OES analysis (Table 1). All the elements apart from the Al, are shown to be homogenously distributed within the sample by SEM-EDS mapping.

Since the O3 and P2 phases have similar crystal structures, SEM analysis was not able to differentiate between the two phases within the material. Therefore, transmission electron microscopy (TEM), in combination with selected area electron diffraction (SAED) was used to further investigate the spatial distribution of the phases within particles on the nanoscale.

Figure 2(a) shows a low magnification bright field TEM overview of the sample, where clear terracing can be observed at the bottom edge of the main grain. Figure 2(b) shows the corresponding selected area electron diffraction (SAED) pattern, with the P2 and O3 reflections annotated in red (top) and blue (bottom), respectively. The high angle annular dark field

(HAADF) image across a terrace and its corresponding FFT in Figure 2(c, d) exhibit essentially identical features to the SAED pattern. The upper half of HAADF image shows the strongest contrast, with the atom columns arranged in a hexagonal motif corresponding to the P2 phase whereas the lower half corresponds to the O3 phase, as shown by the insets. These results therefore demonstrate the coexistence of both phases within the same crystallite, confirming the successful formation of nanoscale intergrown heterostructures in this material.

Electrochemical behaviour

To investigate the sodium storage properties of the O3/P2 biphasic material, the electrochemical performance was studied by galvanostatic charge-discharge testing in half cells using Na^+/Na as the reference and counter electrode and 1 M $NaPF_6$ in EC/DEC as the electrolyte in a potential window of 2.2–4.2 V vs. Na^+/Na at a specific current of 25 mA g^{-1} (Figure 3). The potential profile for the first cycle showed a rapid increase in potential until around 3.25 V, after which the potential increases gently until 4.0 V, where a plateau forms for the remainder of the charge. Two clear regions can be observed upon discharge, above and below 3.0 V, which probably correspond to the Mn^{3+}/Mn^{4+} and Fe^{3+}/Fe^{4+} redox couples, respectively, as reported for other Mn–Fe based sodium layered oxides (Figure 3a).[28–31] As is widely discussed in previous reports, the Cu^{2+}/Cu^{3+} redox couple is also likely to contribute to capacity in the high potential region.[17,32,33] The combined redox processes lead to high initial capacities, with initial charge and discharge capacities of 166 and 140 mAh g^{-1} respectively, giving an acceptable initial coulombic efficiency of 83%. Importantly, the average discharge potential was also high (3.03 V), which gave a high initial discharge energy density of 419 Wh kg^{-1} based on the mass of the active electrode material, which is amongst the highest reported for a Li/Ni/Co-free material and comparable to many Ni-based materials (Figure S3).[16,34–45] The second cycle returns an almost identical discharge capacity of 139 mAh g^{-1}, albeit with a slight decrease in average voltage which originated in the upper potential region. This trend continues in subsequent cycles, with the proportion of capacity stored in the upper voltage region decreasing upon cycling, while the proportion of capacity stored in the lower region increased with increasing cycle number (Figure 3a). This suggests that there is fade associated with lower redox activity of the Fe^{3+}/Fe^{4+} redox couple, while the Mn^{3+}/Mn^{4+} redox couple becomes more active during cycling and increases its contribution to the total capacity stored. This can be observed more clearly in the cyclic voltammetry results (Figure 3c), discussed in the next section. Overall, the compensation of capacity fade linked to the $Fe^{3+}/$
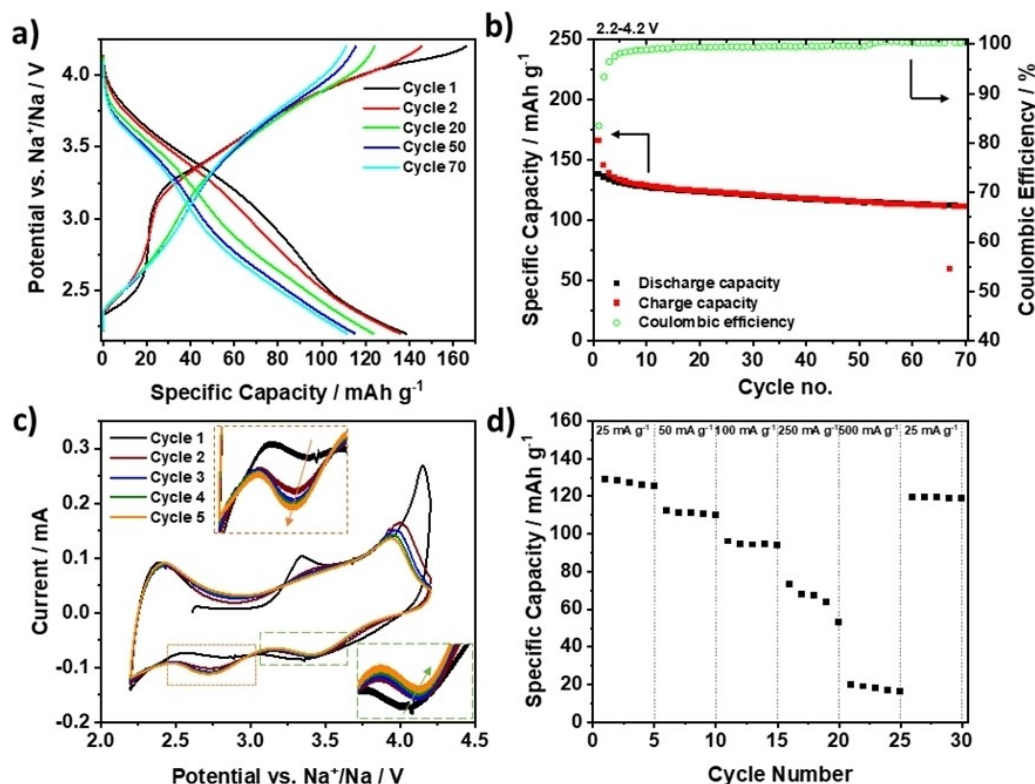

Figure 2. a) Bright field TEM and (b) corresponding SAED pattern confirming the coexistence of O3 and P2 phases. P2 and O3 reflections are annotated in red and blue, respectively. (c,d) HAADF image from the same area with the insets showing the atomic arrangement of the P2 (red) and O3 (blue) regions respectively, and the corresponding FFT showing the same reflections as in (b).

Batteries & Supercaps

Research Article
doi.org/10.1002/batt.202300089

Chemistry Europe
European Chemical
Societies Publishing

Figure 3. Voltage profile for selected cycles of O3/P2-$Na_{0.75}Mn_{0.35}Fe_{0.35}Ti_{0.1}Al_{0.1}Cu_{0.1}O_2$ in a potential window of 2.2–4.2 V cycled in a half cell against Na/Na^+ at a specific current of 25 mA g^{-1}. b) Cycling stability showing the specific capacities and coulombic efficiency across 70 cycles. c) Cyclic voltammograms measured for five cycles in a potential window of 2.2–4.2 V vs. Na^+/Na at a scan rate of 0.030 mV s^{-1}. The insets highlight the activation of the low voltage redox process (Mn based) and simulatneous suppression of the high voltage redox couple (Fe based). d) Discharge capacities resulting from rate capability testing at specific currents of 25, 50, 100, 250 and 500 mA g^{-1} in a potential window of 2.2–4.2 V.

Fe^{4+} redox couple by the Mn^{3+}/Mn^{4+} couple permits high overall capacity retention, with 112 mAh g^{-1} discharge capacity delivered on the 70th discharge, which corresponds to a capacity retention of 80% over 70 cycles (Figure 3b).

To investigate the electrochemical reactions further, cyclic voltammetry (CV) experiments were undertaken using a scan rate of 0.03 mV s^{-1} in a potential window of 2.2–4.2 V vs. Na^+/Na for five cycles (Figure 3c). On the first charging sweep, two clear peaks can be seen at 3.3 V and 4.1 V, with broad peaks at 3.4 V and 2.8 V present on the first discharge, with a tail peak towards the lower potential cut-off at 2.2 V. On subsequent cycles, the charging sweep shows a peak at 2.4 V, a broad weak peak at 3.5 V and a final peak at 4.0 V. On discharge, broad peaks are present at 3.5 V and 2.75 V, with the edge of a final peak appearing towards the lower cut-off at 2.2 V. Based on previous reports, the peaks around 3.5 V probably result from the Fe^{3+}/Fe^{4+} and Cu^{2+}/Cu^{3+} redox couples, while the peaks below 3 V are expected to be due to the Mn^{3+}/Mn^{4+} redox couple.[17,32,33] The peak at a ca. 4 V or above probably corresponds to the gliding of TM layers resulting in phase transformations between layered crystal structures with different stacking sequences. The exact origin of the peaks observed here was investigated in detail by ex situ PXRD and is discussed in later sections. Interestingly, the high potential peaks at or above 3.0 V show a slight decrease in amplitude and potential during cycling, while the peaks below 3.0 V show an increase in

both amplitude and potential. This further suggests that the Mn^{3+}/Mn^{4+} increases its contribution in energy storage during cycling, which compensates for the slight fade observed for the Fe^{3+}/Fe^{4+} redox couple. Similar behaviour has been reported elsewhere for Mn/Fe-based layered oxides.[16,46,47] This compensation allows high capacity and voltage retention (95%, Figure S4) across cycling, while utilising only low cost and abundant elements.

Rate capability tests were performed to evaluate the performance of the material under different charging/discharging times (Figure 3d). The O3/P2 bi-phasic material was cycled between 2.2–4.2 V under increasing specific currents of 25, 50, 100, 250 and 500 mA g^{-1}, before returning to 25 mA g^{-1}, with five cycles conducted at each rate. Discharge capacities of 130, 112, 95, 68 and 20 mAh g^{-1} were obtained respectively, while the capacity recovered to 120 mAh g^{-1} once the current switched back to 25 mA g^{-1}. This shows that the O3-rich mixed phase material could maintain good performance at medium rates up to 100 mA g^{-1}, but at higher specific currents (250 and 500 mA g^{-1}) the indirect Na diffusion pathways caused by the high O3 content in the material result in poor capacity retention at higher rates. O3 materials are known to have poorer Na diffusion kinetics than P2 materials, and also display lower electrical conductivity compared to P2 counterparts. We have previously shown that a P2 rich bi-phasic material displayed much higher rate performance compared to an O3

Batteries & Supercaps

Research Article
doi.org/10.1002/batt.202300089

Chemistry Europe
European Chemical
Societies Publishing

rich version.[48] Therefore, this material is best placed for use in applications which require high energy densities but only require moderate power densities, as a result of the O3-rich nature of the material. Crucially, the lack of significant fade upon returning the specific current to 25 mA g^{-1} after the high-rate testing demonstrates that the bi-phasic material is not damaged by the high cycling currents.

Electrochemical evolution of crystal structure

To understand the effect of the bi-phasic nature of the material on the crystal structure evolution during cycling ex situ XRD was performed on samples extracted at selected states-of-charge (Figure 4a, which shows a typical voltage profile consistent with the coin cell data) during the first cycle, with the results shown in Figure 4(b–d).

For the pristine material, the diffraction pattern displays all major reflections expected in the O3/P2 structure. During charging, all major reflections corresponding to the P2-type phase are retained at each state-of-charge, though minor shifts occur in the location of the reflections. For example, the (002) reflection shifts from 7.26° to 7.25° 2θ upon charging to 3.8 V, with a further shift to lower 2θ to 7.22° and 7.19° 2θ on charging to 4.0 and 4.2 V, respectively. This corresponds to the expansion of the c-axis upon removal of Na$^+$ ions, which results in reduced shielding of the neighbouring O layers by the remaining Na$^+$ ions, causing increased electrostatic repulsion by the O layers, which increased the interlayer spacing upon charging. During discharge, Na is re-inserted into the structure, which reduces the electrostatic repulsion, causing a decrease in

the interlayer spacing, revealed by the shift of the (002) diffraction peak to higher 2θ values 7.25 and 7.28° 2θ when discharged to 3.0 and 2.2 V, respectively. Interestingly, the (002) diffraction peak has shifted to a higher 2θ value at the end of discharge (7.28° 2θ at 2.2 V) compared to the pristine material (7.26° 2θ), which implies that the P2 regions of the material contain more sodium after discharging than before cycling. In contrast, the (102) diffraction peak at 17.8° 2θ shifts to higher angles during charging, corresponding to a decrease in the a-parameter resulting in the shrinkage of the transition metal layers during oxidation. These changes are reversed during discharge, further demonstrating the reversible nature of the structural evolution of the P2-type phase. Overall, the P2 part of the electrode material is retained throughout cycling, corresponding to a solid solution (de)sodiation mechanism. This demonstrates that the inclusion of the P2 phase as part of the intergrown bi-phasic material does indeed stabilise the material, by introducing regions of minimal volume changes, as shown by the limited shifts of the P2 diffraction peaks.

For the O3 part of the material, minimal changes are observed on charging to 3.8 V, with the (003) reflection shifting from 7.33° (pristine) to 7.32° 2θ (charging to 3.8 V), and all major diffraction peaks assigned to the O3-type phase being retained. Upon further charging to 4.0 V, the (003) diffraction peak shifts further to merge with the (002) reflection assigned to the P2 phase, located at ca. 7.24° 2θ. In addition, the intensity ratio between the (104) and (015) reflections changes from the (104) diffraction peak (ca. 18.8° 2θ) showing the higher intensity, which is typical of the O3 structure, to the (015) diffraction peak (ca. 20.1° 2θ) becoming the more intense, which is typically a signature of the P3-type phase.[49] Therefore,
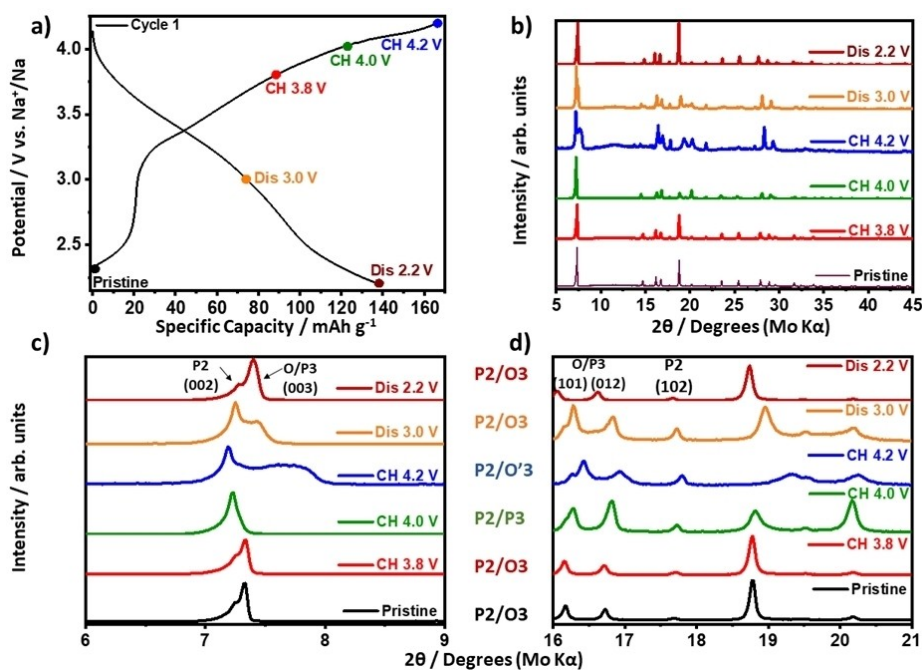

Figure 4. Ex-situ XRD at selected states-of-charge of O3/P2-Na$_{0.75}$Mn$_{0.35}$Fe$_{0.35}$Ti$_{0.1}$Al$_{0.1}$Cu$_{0.1}$O$_2$ in a potential window of 2.2–4.2 V. a) Voltage profile demonstrating the selected states-of-charge. b) Ex-situ XRD patterns at the selected states-of-charge. c) expansion of the low angle region of the diffraction patterns, focusing on the (002/3) diffraction peaks. d) Expansion of the mid-range diffraction pattern, focusing on 16°–21° 2θ.

between 3.8 and 4.0 V, the O3 part of the electrode material begins conversion to the P3 phase, resulting in the electrode consisting of a O3/P3/P2 hybrid structure at 4.0 V, as confirmed by the Rietveld refinements shown in Figure S5 and Table S2. Further charging to 4.2 V results in a severe loss of crystallinity in the O3 part of the crystal structure, with major loss of peak intensity and broadening of the remaining peaks. For example, the (003) peak has broadened to between 7.45 and 7.88° 2θ, which also coincides with a large shrinkage of the c-parameter. This is consistent with a transition from the P3 phase to a distorted O'3 phase, which results in a tri-phasic O'3/P3/P2 material being formed at top-of-charge (Figure S5 and Table S2). Interestingly, the apparent P2 content increased during late charging (from 9% to 14%), resulting from the increased disorder in the material as the P3→O'3 transition occurred. Upon discharge, the O3 peaks gradually reform, demonstrated by the shift of the (003) diffraction peak to 7.45 (3.0 V) and 7.40° 2θ (2.2 V) which correlates with a narrowing and increase in peak intensity, demonstrating that the changes during charging are reversible and that crystallinity is restored. However, the (003) peak remains shifted to slightly higher 2θ values after end of discharge (7.40° 2θ) compared to 7.33° 2θ before cycling, showing that the O3 part of the material remains slightly contracted in the c-direction after discharging. In addition, the P3 phase could not be detected in the material during discharge, showing that the discharge follows a different pathway compared to charging. As was observed for the P2-type phase, the (101) and (012) diffraction peaks, with contributions from the a-parameter, shift to the higher 2θ values during charge (oxidation) and lower 2θ values during discharge (reduction).

Overall, the P2 part of the material is retained throughout cycling, demonstrating solid-solution behaviour, while the O3 regions undergo complex phase transformations of O3→P3→O'3 upon charge which reverses upon discharge. While the a-parameter shows comparable continuous evolution continually during (dis)charging for both the P2 and O3 regions, in high states-of-charge the c-parameter changes in complementary directions, with the P2 region consistently expanding in the c-direction, while the O3-type phase undergoes a contraction. The complementary nature of the changes in the c-parameter between the two phases presumably reduces overall volume change within the bi-phasic material compared to single phase counterparts, which will undergo either an increase (P2) or a decrease (O3) in the c-direction, explaining the impressive cycling stability. Crucially, the O3/P2 bi-phasic structure is reformed after discharging, albeit with minor differences in lattice parameters compared to the pristine material. This, combined with the solid-solution mechanism of the P2-type region, explains the stable cycling performance of the O3/P2 material, and confirms the stabilising role of the P2 phase, which undergoes only minor volume changes during cycling, reducing strain on the electrode material during cycling.

Full cell evaluation

Due to the promising electrochemical performance exhibited by the O3/P2 bi-phasic material in half-cell tests, we constructed a full cell based on the bi-phasic layered oxide as the positive electrode with a high mass loading of 9.5 mg cm^{-2} and a commercial hard carbon as the negative electrode to further demonstrate the practical potential of this material. For reference, performance of the hard carbon in half cells is shown in Figure S6. It demonstrated an initial discharge capacity of 328 mAh g^{-1}, charge capacity of 290 mAh g^{-1} and ICE of 88.4%. After 50 cycles, 85% of the initial discharge capacity was retained. As shown in Figure 5, the full cell achieved high discharge capacities approaching 100 mAh g^{-1}, with a satisfactory ICE of ca. 77%, discharge voltage of up to 2.94 V and excellent cycling stability of 82% over 100 cycles. In addition, the cell displayed high energy efficiencies throughout cycling, up to a maximum of 87%, making it well matched to stationary grid storage type applications which are typically targeted by Na-ion batteries (Figure S7).
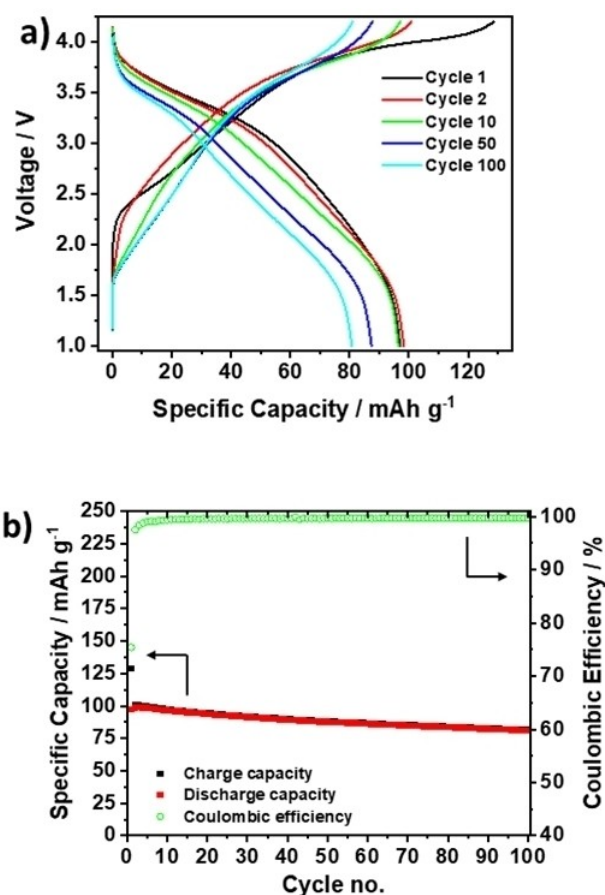
Figure 5. Full cell data of the O3/P2 bi-phasic material against hard carbon. a) Voltage profile of selected cycles. b) Cycling stability data and coulombic efficiency over 100 cycles.

Conclusions

Here we have reported a bi-phasic sodium layered oxide, O3/P2-$Na_{0.75}Mn_{0.35}Fe_{0.35}Ti_{0.1}Al_{0.1}Cu_{0.1}O_2$, as a high energy density Li, Co and Ni free positive electrode for Na-ion batteries. The bi-phasic nature of the material was confirmed by powder XRD, while TEM and SAED studies revealed the two phases co-exist in the same particle as a nanoscale intergrowth. This design provided sufficient Na to deliver high capacities (140 mAh g^{-1}), while keeping the initial Coulombic efficiency below 100%, enabling a high energy density of 419 Wh kg^{-1}, based on the mass of the active positive electrode material, to be achieved in half cells, with high energy efficiency of up to 87% and capacities ca. 100 mAh g^{-1} (292 Wh kg^{-1}) in full cells. Crucially, ex-situ XRD confirmed that the P2 region stabilised the structure by only storing charge via a solid-solution mechanism, which significantly reduced the overall volume changes during cycling compared to the O3 component, which underwent a complex O3→P3→O'3 series of transitions, resulting in stable cycling performance with 80% capacity retention over 70 cycles. Additionally, complementary c-parameter changes were revealed between the two phases, reducing overall lattice strain within the material. Importantly, it was confirmed that the O3/P2 bi-phasic structure was reformed upon discharge, showing the good reversibility of the Na storage processes. The combined use of the Fe^{3+}/Fe^{4+} and Cu^{2+}/Cu^{3+} redox couples raised the charge storage potential, which enabled a high discharge potential (3.03 V in half cells, 2.94 V in full cells), which was remarkably stable over cycling and is key to delivering the high overall energy density. The high performance and mechanistic insights provided here demonstrate the potential for bi-phasic materials to enable a high energy density Na-ion battery utilising only Earth abundant and widely available elements, which will pave the way to the future commercialisation of this technology.

Experimental Section

Synthesis

The target material, $Na_{0.75}Mn_{0.35}Fe_{0.35}Ti_{0.1}Al_{0.1}Cu_{0.1}O_2$ was synthesised using a citric acid assisted sol-gel method. Stoichiometric amounts of sodium nitrate (2 wt.% excess, Alfa Aesar, 99.0%), manganese nitrate (hexahydrate, Alfa Aesar, 98%+), iron nitrate (Alfa Aesar, 98–101%), copper nitrate (Acros Organics, 99%) and aluminium nitrate (Alfa Aesar, 98%) were dissolved in de-ionised (DI) water and stirred for 10 mins. A stoichiometric quantity of TiO_2 nanopowder (anatase, Sigma Aldrich, 99.7%) was then added to the solution under stirring and left to homogenise under stirring for a further 10 mins. Citric acid (Alfa Aesar, 99.5%) was dissolved in a separate beaker (1:1 citric acid to metal molar ratio) and then added to the nitrate solution. The solution was stirred for 2 more hours, before heating to 80°C overnight for gel formation. The gel was then dried at 130°C for 6 h, before being ground in a pestle and mortar and calcined under air for 4 h at 500°C, followed by 12 h at 900°C using a heating/cooling rate of 5°C/min. Once cooled to 250°C, the material was removed and ground in a dry room before transferring to an argon filled glovebox.

Material characterisation

For powder X-ray diffraction (PXRD) studies, glass capillaries were filled and heat sealed and the X-ray diffraction patterns were collected in transmission mode (Debye-Scherrer geometry) using using Mo $K_{\alpha 1}$ radiation, $\lambda = 0.7093$ Å, on a Stoe STADIP diffractometer fitted with a Mythen linear detector. Structures were refined by the Rietveld method using Topas Academic V6. Scanning electron microscopy (SEM) images of as-synthesized materials coupled with Energy Dispersive X-ray spectroscopy (EDS) were recorded on a FEI Scios microscope equipped with an EDAX Octane Plus EDS detector.

Transmission electron microscopy (TEM) and selected area electron diffraction (SAED) were used to investigate the spatial distribution of the two phases on the nanoscale. Samples for transmission electron microscopy (TEM) were prepared by dispersing the powdered sample in n-methyl-2-pyrrolidone (NMP) within an Ar filled glovebox, before drop casting on lacey C/Au grids purchased from Agar Scientific. TEM was performed on an FEI Titan Themis operated at 200 kV with a 4k×4k CETA CMOS camera.

Electrochemical characterization

To investigate the electrochemical performance of the materials, slurries were prepared using the active material, super C65 carbon (Imerys) and Solef 5130 binder (a modified polyvinylidene fluoride (PVDF), Solvay) using a mass ratio of 80:10:10 in n-methyl-2-pyrrolidone (NMP, Alfa Aesar, 99.5%), which was cast onto aluminum foil using a doctor blade. After drying, 10 mm diameter electrode discs were punched and used to prepare CR2325 coin cells (Typical mass loading of ca. 5 mg cm^{-2}). All slurry processing, casting, drying, punching and coin cell assembly was carried out in an argon filled glovebox (MBraun, $O_2 < 0.1$ ppm, $H_2O < 0.1$ ppm). Sodium metal was used as a counter/reference electrode, a glass fiber paper (Whatman, GF/F) was used as the separator and 1 M $NaPF_6$ in ethylene carbonate/diethyl carbonate (1:1) (Kishida) as the electrolyte. Galvanostatic charge/discharge cycling (25 mA g^{-1}, 2.2–4.2 V vs. Na^+/Na) and cyclic voltammetry (0.030 mV s^{-1}, 2.2–4.2 V) were carried out at 30°C using a Biologic BCS-805 battery cycler. For rate capability testing, five cycles were conducted at each specific current of 25, 50, 100, 250 and 500 mA g^{-1}, before returning to 25 mA g^{-1} for a further five cycles. For full cell testing (1–4.2 V, 25 mA g^{-1}, 100 cycles), the O3/P2 positive electrode (9.5 mg cm^{-2}) was paired against a commercial hard carbon, using a 1.3 capacity excess of the hard carbon (88:9:3 active: superC65: binder ratio, supplied coated on C-coated Al foil, cut as 10 mm disks) compared to the layered oxide.

To prepare materials for *ex-situ* characterisation, powder working electrodes were constructed by mixing the active material and super C65 carbon in the mass ratio 75:25 with no binder, using a Swagelok-type cell (ca. 30 mg active material). All other components were the same as used for coin cells, and cells were checked to be within ca. 5% of the expected capacity compared to the coin cell data. Cells were charged to the desired state-of-charge, transferred to an argon-filled glovebox, disassembled, washed using dimethylcarbonate (DMC, Alfa Aesar, 99.0%, anhydrous), and dried overnight under vacuum at room temperature. For ex-situ XRD studies, glass capillaries were filled and heat sealed and the X-ray diffraction patterns were collected in transmission mode (Debye-Scherrer geometry) using Mo $K_{\alpha 1}$ radiation, $\lambda = 0.7093$ Å, on a Stoe STADIP diffractometer fitted with a Mythen linear detector.

Batteries & Supercaps

Research Article
doi.org/10.1002/batt.202300089

Chemistry
Europe

European Chemical
Societies Publishing

Acknowledgements

Conflict of Interests

P.A.M. and A.R.A. declare the international patent "Layered sodium metal oxides for Na-ion batteries" PCT/GB2022/052656. All other authors declare no competing financial interest.

Data Availability Statement

The data that support the findings of this study are available from the corresponding author upon reasonable request.

[1] I. Hasa, S. Mariyappan, D. Saurel, P. Adelhelm, A. Y. Koposov, C. Masquelier, L. Croguennec, M. Casas-Cabanas, *J. Power Sources* **2021**, *482*, 228872.
[2] P. K. Nayak, L. Yang, W. Brehm, P. Adelhelm, *Angew. Chem. Int. Ed.* **2018**, *57*, 102–120.
[3] J. Y. Hwang, S. T. Myung, Y. K. Sun, *Chem. Soc. Rev.* **2017**, *46*, 3529–3614.
[4] C. Delmas, C. Fouassier, P. Hagenmuller, *Phys. B + C* **1980**, *99*, 81–85.
[5] J. Deng, W. Bin Luo, S. L. Chou, H. K. Liu, S. X. Dou, *Adv. Energy Mater.* **2018**, *8*, 1701428.
[6] C. Delmas, D. Carlier, M. Guignard, *Adv. Energy Mater.* **2021**, *11*, 2001201.
[7] S. Xu, J. Wu, E. Hu, Q. Li, J. Zhang, Y. Wang, E. Stavitski, L. Jiang, X. Rong, X. Yu, W. Yang, X.-Q. Yang, L. Chen, Y.-S. Hu, *J. Mater. Chem. A* **2018**, *6*, 20795–20803.
[8] A. Rudola, A. J. R. Rennie, R. Heap, S. S. Meysami, A. Lowbridge, F. Mazzali, R. Sayers, C. J. Wright, J. Barker, *J. Mater. Chem. A* **2021**, *9*, 8279–8302.
[9] G. Singh, N. Tapia-Ruiz, J. M. L. del Amo, U. Maitra, J. W. Somerville, A. R. Armstrong, J. M. de Ilarduya, T. Rojo, P. G. Bruce, *Chem. Mater.* **2016**, *28*, 5087–5094.
[10] Q. Wang, S. Mariyappan, J. Vergnet, A. M. Abakumov, G. Rousse, F. Rabuel, M. Chakir, J.-M. Tarascon, *Adv. Energy Mater.* **2019**, *9*, 1901785.
[11] C. Vaalma, D. Buchholz, M. Weil, S. Passerini, *Nat. Rev. Mater.* **2018**, *3*, 1–11.
[12] N. Yabuuchi, M. Kajiyama, J. Iwatate, H. Nishikawa, S. Hitomi, R. Okuyama, R. Usui, Y. Yamada, S. Komaba, *Nat. Mater.* **2012**, *11*, 512–7.
[13] C. W. Mason, F. Lange, K. Saravanan, F. Lin, D. Nordlund, *ECS Electrochem. Lett.* **2015**, *4*, A41.
[14] S. Mariyappan, T. Marchandier, F. Rabuel, A. Iadecola, G. Rousse, A. V. Morozov, A. M. Abakumov, J.-M. Tarascon, *Chem. Mater.* **2020**, *32*, 1657–1666.
[15] Y. Zhang, S. Kim, G. Feng, Y. Wang, L. Liu, G. Ceder, X. Li, *J. Electrochem. Soc.* **2018**, *165*, A1184–A1192.
[16] Y. Yoda, K. Kubota, K. Kuroki, S. Suzuki, K. Yamanaka, T. Yaji, S. Amagasa, Y. Yamada, T. Ohta, S. Komaba, *Small* **2020**, *16*, 2006483.
[17] Y. Li, Z. Yang, S. Xu, L. Mu, L. Gu, Y. S. Hu, H. Li, L. Chen, *Adv. Sci.* DOI:10.1002/advs.201500031.
[18] L. Mu, S. Xu, Y. Li, Y. S. Hu, H. Li, L. Chen, X. Huang, *Adv. Mater.* **2015**, *27*, 6928–6933.
[19] A. Tripathi, A. Rudola, S. R. Gajjela, S. Xi, P. Balaya, *J. Mater. Chem. A* **2019**, *7*, 25944–25960.
[20] E. Lee, J. Lu, Y. Ren, X. Luo, X. Zhang, J. Wen, D. Miller, A. DeWahl, S. Hackney, B. Key, D. Kim, M. D. Slater, C. S. Johnson, *Adv. Energy Mater.* **2014**, *4*, 1400458.
[21] S. Guo, P. Liu, H. Yu, Y. Zhu, M. Chen, M. Ishida, H. Zhou, *Angew. Chem. Int. Ed.* **2015**, *54*, 5894–5899.
[22] Z. Y. Li, J. Zhang, R. Gao, H. Zhang, L. Zheng, Z. Hu, X. Liu, *J. Phys. Chem. C* **2016**, *120*, 9007–9016.
[23] X. Qi, L. Liu, N. Song, F. Gao, K. Yang, Y. Lu, H. Yang, Y. S. Hu, Z. H. Cheng, L. Chen, *ACS Appl. Mater. Interfaces* **2017**, *9*, 40215–40223.
[24] D. Zhou, W. Huang, X. Lv, F. Zhao, *J. Power Sources* **2019**, *421*, 147–155.
[25] M. Bianchini, E. Gonzalo, N. E. Drewett, N. Ortiz-Vitoriano, J. M. López Del Amo, F. J. Bonilla, B. Acebedo, T. Rojo, *J. Mater. Chem. A* **2018**, *6*, 3552–3559.
[26] L. Yang, J. M. L. del Amo, Z. Shadike, S. M. Bak, F. Bonilla, M. Galceran, P. K. Nayak, J. R. Buchheim, X. Q. Yang, T. Rojo, P. Adelhelm, *Adv. Funct. Mater.* **2020**, *30*, 2003364.
[27] B. H. Toby, R. B. Von Dreele, *J. Appl. Cryst.* **2013**, *46*, 544–549.
[28] N. Van Nghia, P.-W. Ou, I.-M. Hung, *Electrochim. Acta* **2015**, *161*, 63–71.
[29] W. M. Dose, N. Sharma, J. C. Pramudita, M. Avdeev, E. Gonzalo, T. Rojo, *Chem. Mater.* **2018**, *30*, 7503–7510.
[30] E. Talaie, S. Y. Kim, N. Chen, L. F. Nazar, *Chem. Mater.* **2017**, *29*, 6684–6697.
[31] B. M. de Boisse, D. Carlier, M. Guignard, E. Guerin, M. Duttine, A. Wattiaux, C. Delmas, *Chem. Mater.* **2018**, *30*, 7672–7681.
[32] W. Kang, Z. Zhang, P. K. Lee, T. W. Ng, W. Li, Y. Tang, W. Zhang, C. S. Lee, D. Y. Wai Yu, *J. Mater. Chem. A* **2015**, *3*, 22846–22852.
[33] Z. Y. Li, H. Wang, W. Yang, J. Yang, L. Zheng, D. Chen, K. Sun, S. Han, X. Liu, *ACS Appl. Mater. Interfaces* **2018**, *10*, 1707–1718.
[34] C. Zhao, Z. Yao, Q. Wang, H. Li, J. Wang, M. Liu, S. Ganapathy, Y. Lu, J. Cabana, B. Li, X. Bai, A. Aspuru-Guzik, M. Wagemaker, L. Chen, Y. S. Hu, *J. Am. Chem. Soc.* **2020**, *142*, 5742–5750.
[35] A. Tripathi, S. Xi, S. R. Gajjela, P. Balaya, *Chem. Commun.* **2020**, *56*, 10686–10689.
[36] A. Tripathi, A. Rudola, S. R. Gajjela, S. Xi, P. Balaya, *J. Mater. Chem. A* **2019**, *7*, 25944–25960.
[37] J. L. Yue, W. W. Yin, M. H. Cao, S. Zulipiya, Y. N. Zhou, Z. W. Fu, *Chem. Commun.* **2015**, *51*, 15712–15715.
[38] X. Sun, X. Jin, C. Y. Zhang, J. W. Wen, Y. Shao, Y. Zang, C. H. Chen, *J. Mater. Chem. A* **2014**, *2*, 17268–17271.
[39] S. M. Oh, S. T. Myung, C. S. Yoon, J. Lu, J. Hassoun, B. Scrosati, K. Amine, Y. K. Sun, *Nano Lett.* **2014**, *14*, 1620–1626.
[40] N. Yabuuchi, M. Yano, H. Yoshida, S. Kuze, S. Komaba, *J. Electrochem. Soc.* **2013**, *160*, A3131–A3137.
[41] D. Kim, E. Lee, M. Slater, W. Lu, S. Rood, C. S. Johnson, *Electrochem. Commun.* **2012**, *18*, 66–69.
[42] H. R. Yao, P. F. Wang, Y. Wang, X. Yu, Y. X. Yin, Y. G. Guo, *Adv. Energy Mater.* **2017**, *7*, 1700189.
[43] L. Mu, S. Xu, Y. Li, Y. S. Hu, H. Li, L. Chen, X. Huang, *Adv. Mater.* **2015**, *27*, 6928–6933.
[44] Y. Li, Z. Yang, S. Xu, L. Mu, L. Gu, Y. S. Hu, H. Li, L. Chen, *Adv. Sci.* **2015**, *2*, 1500031.
[45] P. F. Wang, Y. You, Y. X. Yin, Y. S. Wang, L. J. Wan, L. Gu, Y. G. Guo, *Angew. Chem. Int. Ed.* **2016**, *55*, 7445–7449.
[46] S. Xu, J. Wu, E. Hu, Q. Li, J. Zhang, Y. Wang, E. Stavitski, L. Jiang, X. Rong, X. Yu, W. Yang, X—Q. Yang, L. Chen, Y—S. Hu, *J. Mater. Chem. A* **2018**, *6*, 20795–20803.
[47] S. G. Lim, M—S Kwon, T. Kim, H. Kim, S. Lee, J. Lim, H. Kim, K. T. Lee, *ACS Appl. Mater. Interfaces* **2022**, *14*, 33120–33129.
[48] P. A. Maughan, A. B. Naden, J. T. S. Irvine, A. R. Armstrong, *Commun. Mater.* **2023**,, 6.
[49] T. Risthaus, L. Chen, J. Wang, J. Li, D. Zhou, L. Zhang, D. Ning, X. Cao, X. Zhang, G. Schumacher, M. Winter, E. Paillard, J. Li, *Chem. Mater.* **2019**, *31*, 5376–5383.

RESEARCH ARTICLE

Biphasic material: A bi-phasic sodium layered oxide material, O3/P2-$Na_{0.75}Mn_{0.35}Fe_{0.35}Ti_{0.1}Al_{0.1}Cu_{0.1}O_2$, is described which delivers energy densities up to 420 Wh kg^{-1}, discharge potential of 2.94 V in full cells, and excellent capacity retention. This demonstrates the potential for bi-phasic materials to enable a high energy density Na-ion battery utilising only Earth abundant and widely available elements.
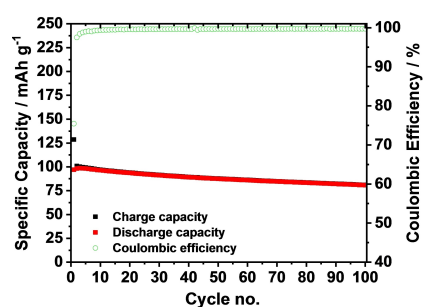
Dr. P. A. Maughan, Dr. A. B. Naden, Prof. J. T. S. Irvine, Dr. A. R. Armstrong*

1 – 9

High Energy Density Li/Ni/Co-Free O3/P2 Sodium Layered Oxide Intergrowth for Sodium-Ion Batteries